LDIA
International Symposium on
Linear Drives for Industry Applications

Hangzhou
2013

The Ninth International Symposium on Linear Drives for Industry Applications

Proceedings

Organized by:

Zhejiang University

Co-organized by:

Linear Motor Institute, Chinese Electrotechnical Society

Institute of Electrical Engineering, Chinese Academy of Science

Technical Co-sponsor:

IEEE Industry Applications Society

Supporters:

National Natural Science Foundation of China

Henful

Design of a Contactless Power Supply for Magnetically Levitated Elevator Systems integrated into the Guide Rail

R. Appunn, A. K. Putri and K. Hameyer
Institute of Electrical Machines, RWTH Aachen University, Germany
Email: ruediger.appunn@iem.rwth-aachen.de

***Abstract*--A contactless energy transmission system is essential to supply onboard systems of magnetically levitated vehicles without physical contact to the guide rail. This paper introduces a contactless power supply (CPS) where the primary is integrated into the guide rail of an electromagnetic guiding system (MGS). The secondary is mounted onboard the elevator car. The advantages of this system when compared to existing energy transmission systems are the low requirement of construction space and reduced costs.**

***Index Terms*—contactless energy transmission, electromagnetic guiding system, magnetically levitated elevator, ferro-magnetic material at high frequency**

I. INTRODUCTION

Electromagnetically levitated vehicles require a contactless power transmission to overcome the air gap between a fixed guide way and the moving part without sliding contacts or travelling cables to power onboard components. Hereby their benefits e.g. wearless operation, are augmented. Fast moving vehicles, e.g. maglev trains are able to consume power via harmonics induced by the propulsion device mounted to the guide way [1]. A slow moving elevator requires a separate transmission system which yields further cost and requires additional construction space.

In contrast to apply a continuous energy transmission, which means an increase amount of copper alongside the track, a discrete charging of an onboard energy storage system is possible. In automotive sector one can find such applications [2, 3]. Previous studies to minimize both, cost and space are based on an integrated solution of guiding and power transmission, where the same flux path is used for both operation [4, 5]. This paper presents a topology, in which a soft-ferrite actuator with coils around its lateral arms is integrated into in the guide rail of a MGS. An identical secondary actuator is mounted onboard the elevator car. When the position of primary and secondary actuators match, a power transmission is established and a battery on the elevator can be charged. The integrated primary actuator disturbs the guiding forces of the omega shaped actuators [6] when passing over them. So a careful design process regarding power transfer capability and force reduction is essential.

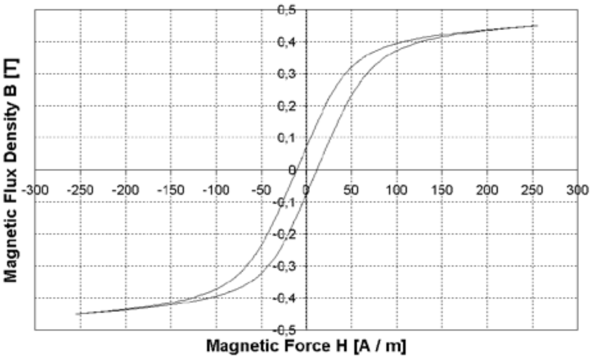

Fig. 1. B-H-graph of the soft ferrite ceramic.

II. DESIGN PROCESS

The design process of the transmission path is divided into the following chapters. First a characterization of the utilized soft ferrite material is presented. The electromagnetic design, including analytical and numeric approaches follows. An electrical design finalizes the process.

·

A. Material characterization

A soft ferrite ceramic is chosen for the transmission actuators. To identify the electromagnetic parameters of this material, two identical u-shaped probes are wound with coils and measured at the core tester of a material test bench at the institute.

First the magnetic material characteristics at a frequency of 50 Hz are identified. Figure 1 shows the BH-diagram. It can be seen that saturation occurs at a flux density of B = 0.45 T. The saturation of the guide rail, which is made of solid steel, is B = 1.8 T. The significantly lower saturation of the soft ferrite will result in a force drop, when the guiding actuator passes the primary actuator integrated into the guide rail, since the guiding force is quadratically proportional to the flux density. This fact is a design limitation and will be discussed in the further design process.

Inductive transmission systems normally operate in a high frequency region from 10 kHz up to several hundred kHz [7]. On the one hand the deliverable power is proportional to the frequency, on the other hand material losses increase with the frequency, as well. To determine the operation frequency of the power supply, the specific

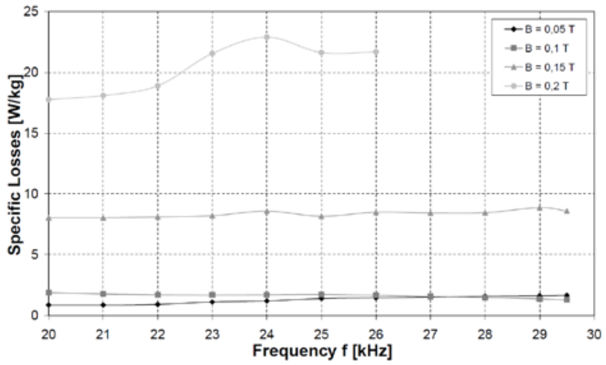

Fig. 2. Specific losses with respect to frequency and flux density.

losses of the material are measured. Since the audible region of the human ear is approximately from 20 Hz to 20 kHz, the measurement is performed from 20 kHz to 30 kHz. Hereby the amplitude of the flux density is varied as well. Figure 2 depicts the specific material losses with respect to the frequency at different flux densities. It can be seen that the dependency of the flux density is higher than the dependency of the frequency.

A maximal flux density of 0.1 T is defined to minimize core losses and an operation frequency of 25 kHz is chosen regarding to switching losses of power electronic components. Table I shows the magnetic material parameter at this working point.

TABLE I
PARAMETERS OF THE SOFT FERRITE AT 25 KHZ AND 0.1 T.

Specific losses	1.73 W/kg
Relative permeability	3398

B. Electromagnetic design

After material characterization the electromagnetic design of the transmission path is done. By analytical magnetic circuit calculations different actuator types are considered. The final design is configured using numerical finite element methods. The maximum current of primary and secondary coils is set to 10 A, standard electrical devices can be used this way.

1) Analytical design

Starting from the first Maxwell equation:

$$\oint_{\partial C} \vec{H} \cdot d\vec{s} = \iint_{C} \vec{S} \cdot d\vec{A} \qquad (1)$$

The flux distribution in different actuator geometries can be calculated by means of magnetic circuit analysis. Here three topologies are considered: U-shaped, E-shaped and C-shaped actuators.

The fact that the primary actuator is integrated into the guide rail is a limitation for the geometrical dimensions of the transmission actuator. Figure 3 shows the area which is reserved for the primary actuator (U- and E-shaped). For an optimal magnetic coupling, it has to be placed directly opposite to the central yoke of the omega actuator. The low saturation of the flux density limits the area occupied by the actuators, since the guiding force drops drastically. In contrast the primary of the C-shaped actuator can be placed in a way the guiding force is not disturbed.

With this constrains an analytical design is done for all three actuators. Table II lists the parameters of the actuators. As a result all actuators are able to transmit the required power of 250 W with a flux density not higher than 0.1 T. Due to the least weight and the simple geometry, two identical U-shaped cores are chosen as primary and secondary actuators.

TABLE II
COMPARISON OF THE ACTUATOR SHAPES

	U-core	E-core	C-core
Weight m [kg]	0.65	0.96	1.1
Flux density B_{max} [T]	0.083	0.069	0.08
Power P [W]	271.5	272.7	254.5

2) Numerical design

Using finite element methods a numerical design follows the analytical considerations. The FEM software pyMOOSE [8] which is developed at the IEM is uses for the calculations. First the disturbance of the guiding forces due to the soft ferrite is calculated. Afterwards the sensitivity of the mutual inductance M due to positioning errors is regarded. In contrast to the analytical calculations leakage flux is not neglected anymore.

As a constrain the maximal force drop of the guiding force at maximum magnetomotive force (MMF) of 2000 At has to be less than 15 %. Herewith the geometric parameters found in the analytical approach are recalculated to fulfill this criterion. Figure 4 shows the FE model of the primary actuator within the guide rail surrounded by the omega actuator. The deviation of the guiding force in y-direction with respect to the MMF is depicted in figure 5. The calculation is done for two positions of the actuator, at the center and at the edge of the U-shaped actuator. It can be seen that the deviation in higher at the edge, since there is less iron opposite to the omega actuator in this position. The maximal force drop is 14.35 %, so the criterion is fulfilled. The same analysis is done for the deviation in x-direction. Simulations show a deviation not higher than 10 %. Herewith A topology with a minimal disturbance of the guiding force is found.

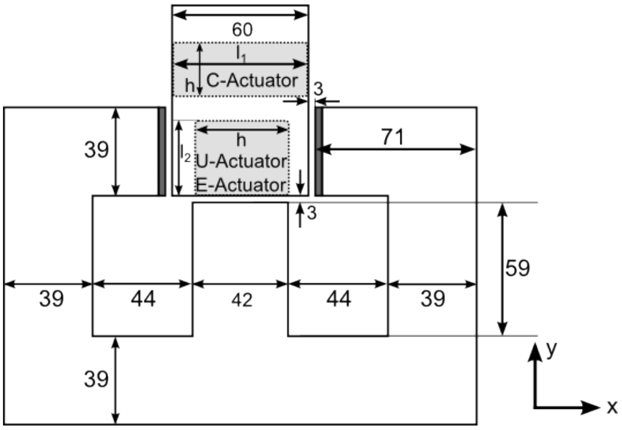

Fig. 3. The guiding actuator surrounding the guide rail with the area reserved for the different transmission actuators.

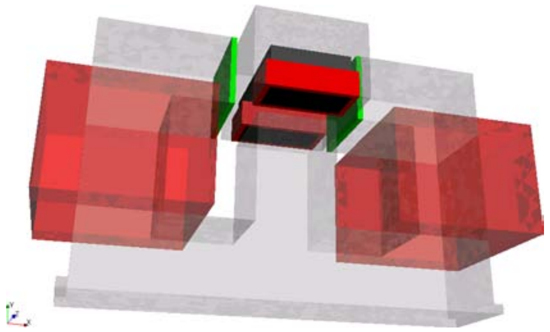

Fig. 4. Omega shaped guiding actuator passing primary transmission actuator.

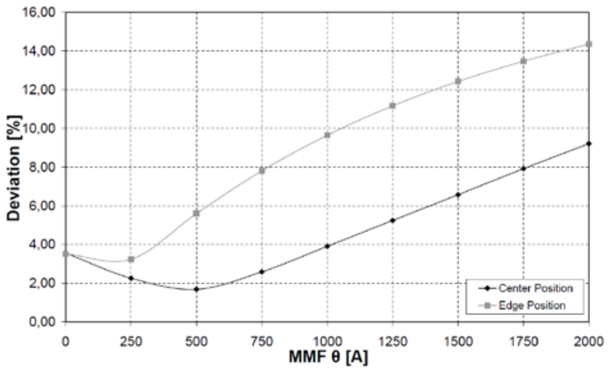

Fig. 5. Deviation of the guiding force in y-direction.

After a design regarding to a minimal disturbance of the guiding force is found the transmission capability of the actuator is investigated. From finite element computation the inductance matrix of the topology is extracted. The following equation describes the transmission path:

$$\begin{bmatrix}u_1\\ u_2\end{bmatrix} = j\omega\cdot\begin{bmatrix}L_p & M_{12}\\ M_{21} & L_s\end{bmatrix}\cdot\begin{bmatrix}i_p\\ i_s\end{bmatrix} = j\omega\mathbf{L}\cdot\begin{bmatrix}i_p\\ i_s\end{bmatrix} \qquad (2)$$

Where u_1 and u_2 are the sums of the voltages over the inductances L_p and L_s and the reflected voltage u_p and the induced voltages u_s, respectively.

Ideally $M_{12} = M_{21} = M$. From analytical calculations the mutual inductance $M = 34.12\ \mu H$, where the FEM extractions gives $M = 39.52\ \mu H$. This deviation can be explained with the flux distribution shown in figure 6.

Here the flux density in both primary and secondary yokes applying a nominal primary current of 10 A is shown. In contrast to the analytical calculation the flux density is not constant at 0.58 T. It varies up to 0.1 T in the numerical calculation. That is the reason for the discrepancy in the mutual inductance. The coupling coefficient $k = 0.83$ which is a quite high value for a loosely coupled transmission system [9].

The tolerance of the inductive power supply due to positioning errors is considered in the following paragraph. The secondary actuator is displaced 1 mm in each of the three spatial directions. The deviation of the mutual inductance with respect to y- and z-direction is shown in figure 7.

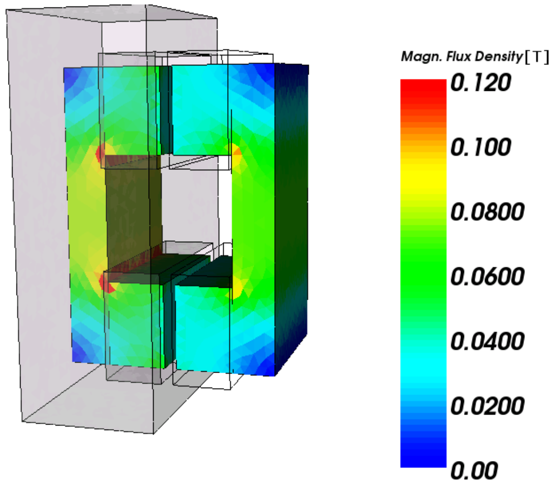

Fig. 6. Magnetic flux density of the aligned transmission actuators.

This deviation is very small. Whereas a displacement in x-direction about 1 mm, which resembles an increase of the air gap, results in a decrease of the mutual inductance of 30 % (compare figure 8).

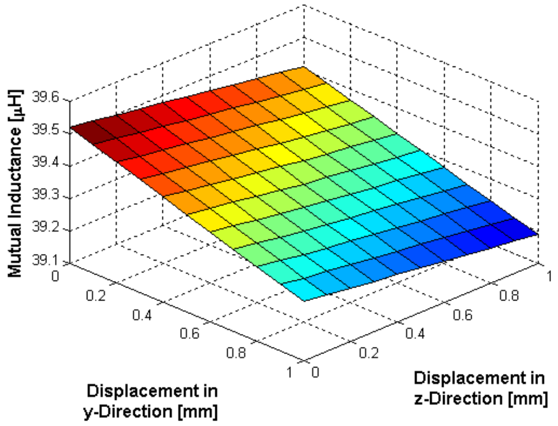

Fig. 7. Deviation of the mutual inductance in y- and z-direction.

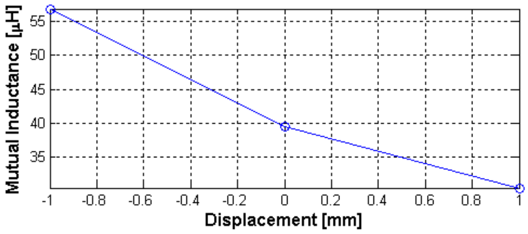

Fig. 8. Deviation of the mutual inductance in x-direction.

C. *Electrical design*

After the geometry of the actuator is devised, a reactive power compensation has to be designed. Four compensation topologies can be utilized: serial-serial, serial-parallel, parallel-serial and parallel-parallel. In this chapter the most appropriate one for the elevator application is deduced.

Using the electric circuit simulator PLECS [10], the transmission path can be described by its lumped parameters, i.e. the inductance matrix **L** and the winding resistances R_p and R_s. A transformer π-equivalent circuit can be used. The four compensation topologies are simulated. Since the transmission system is designed for loading an onboard battery, a load resistance $R_{load} = 5\ \Omega$ is modeled. This reflects the inner resistance of 50 lithium-polymer battery-cells connected in series (including a dc-converter) which can provide 185 V to power the guiding actuators an onboard electronics.

Without reactive power compensation the maximum transmittable power equals:

$$P_{\max} = U^2_{s,oc} \cdot \frac{R_{load}}{R^2_{load} + (\omega L_s)^2} \ . \qquad (3)$$

To increase the deliverable power, the secondary inductance L_s has to be compensated. Herewith the induced voltage u_s is directly applied on the load resistance R_{load}. The choice of the secondary compensation depends on the purpose of the energy transmission. Using a serial compensation, the impedance of the secondary is neutralized and the secondary voltage u_s becomes load independent. Herewith the compensated secondary resembles a voltage source and $u_s = u_{s,oc}$. This compensation topology is often used when feeding a DC-link [11].

Using a parallel compensation, the admittance of the secondary is neutralized and the secondary current i_s becomes load independent. The secondary resembles a current source with $i_s = i_{s,sc}$ which can be used for battery charging [12].

The primary compensation compensates the primary inductance L_p and the imaginary part of the reflected resistance $\Im\{\underline{Z}_r\}$. This reduces the apparent power which has to be delivered by the source. The choice of the compensation topology depends on the form of the primary coil. Considering a long primary placed alongside a track, the voltage drop is very high. For this application a serial compensation is applicable, reducing the input voltage which has to be delivered by the source [7]. For a concentrated coil a high current is often required, where a parallel compensation gives advantages since the input current can be reduced [13]. The derivation of the compensation capacitances is described in literature [14, 15].

The ratio between reactive power on primary and secondary, respectively and the transmittable active power is called quality factor. The quality factor of the primary and secondary is defined as:

$$Q_p = \frac{i_p^2 \omega L_p}{i_p^2 \Re\{\underline{Z}_r\}} \text{ and } Q_s = \frac{i_s^2 \omega L_s}{i_s^2 \Re\{\underline{Z}_r\}} \ . \qquad (4)$$

For system stability it is essential that $Q_p >> Q_s$ [16]. For the inductive power supply regarded in this paper a serial secondary compensation will result in an instable system. Therefore the secondary will be compensated in parallel. To choose the primary compensation topology, various simulations are done. In addition to the nominal operation, deviations are considered as well. On the one hand a variation of the load resistance is computed. This occurs if the state of charge of the battery changes. On the other hand position displacements resulting from the MGS are regarded. Figure 9 depicts the deviation of the efficiency for both compensation topologies with respect to the load resistance R_{load}. The parallel-parallel topology has a higher efficiency over a larger region. Finally the sensitivity of tolerances in the confected capacitors is regarded. The parallel-parallel topology is less sensitive to deviations from resonance.

Considering all this aspects the most appropriate compensation topology is the parallel-parallel.

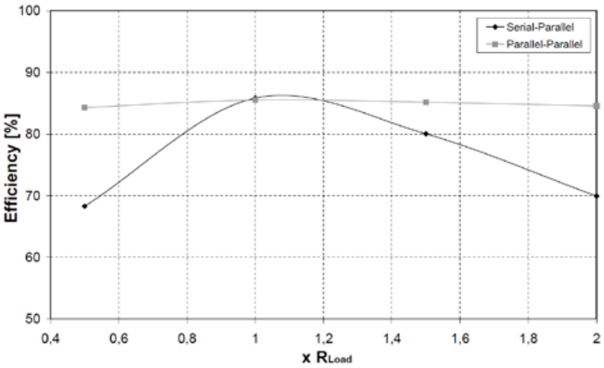

Fig. 9. Efficiency of both compensation topologies with respect to the load resistance.

III. EXPERIMENTAL VERIFICATION

To evaluate the design chain, a prototype of the transmission path is built up. Figure 10 depicts the primary actuator integrated into the guide rail. The compensated inductive power supply is measured in the working point and deviations are regarded as well. The parameters of the electric elements are listed in table IV.

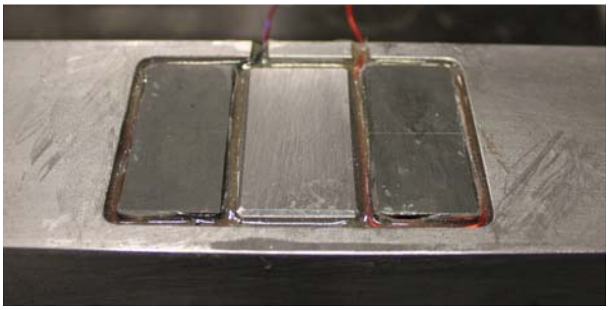

Fig. 10. Primary actuator integrated into the guide rail.

TABLE III
ELECTRICAL DATA OF THE TRANSMISSION PATH

Filter inductance L_{fi}	16.5 µH
Filter capacitance C_{fi}	1.66 µF
Filter frequency f_g	30.4 kHz
Winding resistances R_p, R_s	8.62 mΩ
Primary capacitance C_p	861 nF
Secondary capacitance C_s	849 nF
Load resistance R_{load}	5 Ω

A. Measurement of the inductance matrix

From no-load measurements the inductance matrix can be determined. Table IV compares the simulated and measured values. The mutual inductance and the secondary self inductance show a good accordance. The primary self inductance is higher compared to the simulated value. Since the primary actuator is buried into the iron guide rail, the leakage flux $\Phi_{\sigma,1}$ and with it the primary inductances increases. Regarding the phase shift between voltage and current at no load, an angle of 86° is measured. This means hysteresis and eddy current losses in the soft ferrite are very small and can be neglected in the modeling process.

TABLE IV
MEASURED AND SIMULATED INDUCTANCES

	simulated	measured	Deviation
Primary self inductance L_p	47.75µH	56.11µH	14.9%
Secondary self inductance L_s	47.73µH	52.18µH	8.5%
Mutual inductance M	39.53µH	38.7µH	2.1%

B. Additional losses of the guide rail

From short circuit measurements a phase shift of 77° is observed. In this operation point additional losses occur in the iron guide rail. To analyze this phenomenon additional FEM calculations are done with primary and secondary windings powered by 10 A in opposite direction. From figure 11 it can be seen that the flux is displaced from the primary actuator into the iron rail. The flux no longer penetrates the soft composite yoke, completely. There is a high leakage component which penetrates the iron in between the yokes of the primary actuator. Herewith additional losses occur and have to be regarded in the modeling of the transmission path.

Since these losses depend on the leakage flux and do not occur in no-load operation, two additional electrical elements are placed in the circuit model (compare figure 12). The first element is the leakage inductance of the iron $L_{\sigma Fe}$ which models an increase of the leakage flux. The second element is the iron resistance $R_{\sigma Fe}$, which models the active power losses in the rail. Both parameters are highly nonlinear and determined by measurements in various operation points. Figures 13 and 14 depict the leakage inductance $L_{\sigma Fe}$ and the iron resistance $R_{\sigma Fe}$ with respect to the primary current I_p and the load resistance R_{load}. Regarding the current dependency, the value of the elements increases with approximately $1-e^{-x}$, i.e. with increasing load the value decreases. At no load the value of the additional elements is zero and they have no influence to the system.

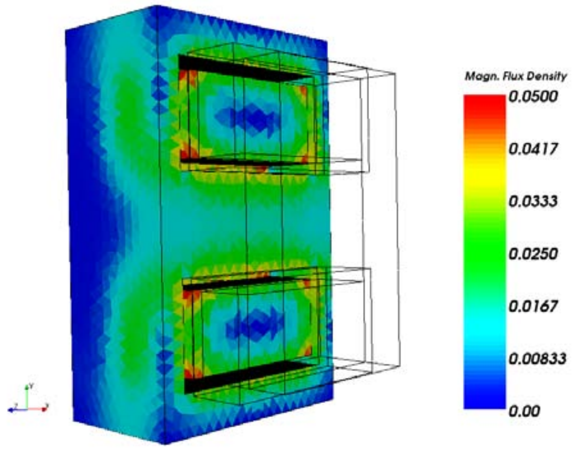

Fig. 11. Magnetic flux density within the guide rail applying opposite currents on primary and secondary.

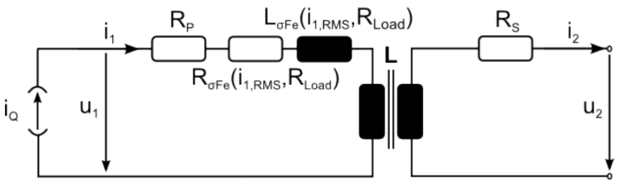

Fig. 12. Equivalent circuit for the integrated CPS.

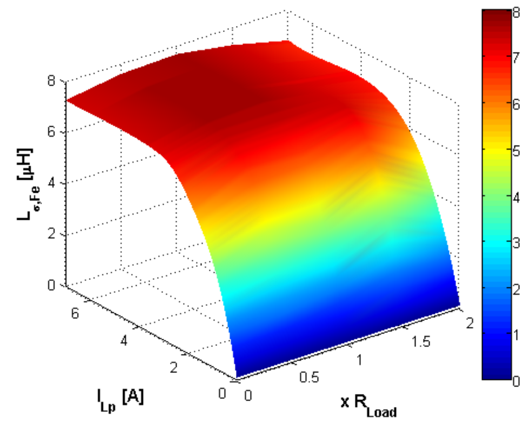

Fig. 13. Additional leakage inductance of the guide rail.

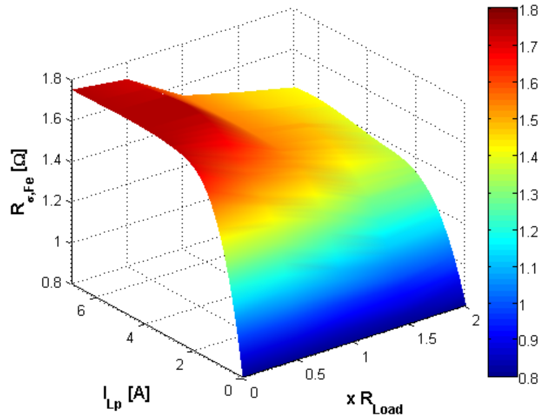

Fig. 14. Additional iron resistance of the guide rail.

C. Nominal operation

Various operation points are measured at the prototype test bench. The output power is proportional to the load resistance, since the parallel compensated secondary resembles a current source. The output current does not depend on the input current, but on the current of the primary coil. The output power is reciprocally proportional to the air gap. The mutual inductance decreases with a larger air gap and the leakage flux increases. Figure 15 depicts the efficiency of the CPS with respect to air gap displacements and load variations. The maximum efficiency is 55 % at nominal load and an air gap of 2 mm. Comparing simulated and measured efficiency the modeling characterizes the CPS quite well with a maximal deviation is 11.5 %. Figure 16 shows the deviation with respect to air gap displacements and load variations.

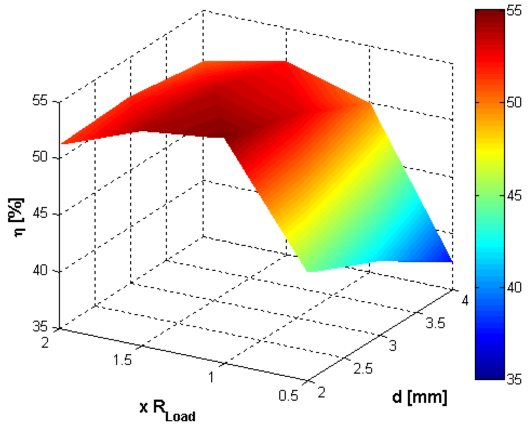

Fig. 15. Efficiency of the integrated CPS.

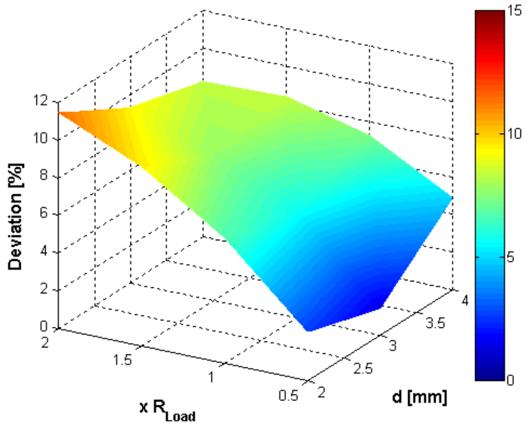

Fig. 16. Deviation of the efficiency between measurement and simulation.

IV. CONCLUSIONS

In this paper an inductive power transmission for a vertical transportation vehicle is introduced. The primary transmission actuator is integrated into the guide rail of a magnetic guiding system. Hereby construction space and costs can be reduced. Starting from analytical magnetic circuit calculations the design process is described. The power transfer capability of the system is discussed in detail and the disturbance of the linear guiding is analyzed. Parameter extraction is done using finite element methods and analytical models. The dynamic system behavior is observed in a circuit simulator. A prototype is built up and measurement results verify the modeling, using non linear circuit elements. In contrast to an air surrounded transmission path, the efficiency is lower due to additional losses in the guide rail.

REFERENCES

[1] J.-Y. Lee, I.-J. Lee, J.-W. Kim, J.-H. Chang, D.-H. Kang, S.-U. Chung and J.-P. Hong, “Contactless power transfer system combined with linear electric machine.” *Proc. of 8th Int. Conf. on Electrical Machines and Systems (ICEMS 2007)*, Seoul (Korea), 2007, pp. 1544 –1548.

[2] B. Schmuelling, S.G. Cimen, T. Vosshagen, F. Turki, “Layout and operation of a non-contact charging system for electric vehicles.” *Proc. of 15th Int. Conf. on Power Electronics and Motion Control (EPE/PEMC 2012)*, Novi Sad (Serbia), Sept. 2012, pp.LS4d.4-1-LS4d.4-7.

[3] M. Budhia, G. Covic, J. Boys, “A new IPT magnetic coupler for electric vehicle charging systems.” *Proc. of 36th Annual Conference on IEEE Industrial Electronics Society (IECON 2010)*, Phoenix (USA), Nov. 2010 pp.2487-2492.

[4] R. Appunn, B. Riemer, and K. Hameyer, “Contactless power supply for magnetically levitated elevator systems.” *Proc. of 20th Int. Conf. on Electrical Machines (ICEM 2012)*, Marseille (France), Sept. 2012, pp. 600–605.

[5] B. Schmülling and K. Hameyer, “PowerTRACE – a Novel Power Transmission and Actuator Entity.” *Proc. of 20th Int. Conf. on Magnetically Levitated Systems and Linear Drives (MAGLEV 2008)*, San Diego (USA), Dec. 2008, pp. 15–18.

[6] R. Appunn, B. Schmülling, and K. Hameyer, “Electromagnetic Guiding of Vertical Transportation Vehicles: Experimental Evaluation,” *IEEE Trans. on Industrial Electronics*, vol. 57, pp. 335–343, Jan. 2010.

[7] J.M. Barnard, J.A. Ferreira, J.D. Van Wyk, “Sliding transformers for linear contactless power delivery,” *IEEE Trans. on Industrial Electronics*, vol.44, no.6, pp.774-779, Dec. 1997.

[8] E. Lange, F. Henrotte, and K. Hameyer, “An efficient field-circuit coupling based on a temporary linearization of fe electrical machine models,” *IEEE Trans. on Magnetics*, vol. 45, no. 3, pp. 1258-1261, 2009.

[9] C.-S. Wang, O. Stielau, and G. Covic, “Design considerations for a contactless electric vehicle battery charger,” *IEEE Trans. on Industrial Electronics*, vol. 52, no. 5, pp. 1308 – 1314, 2005.

[10] J. Allmeling and W. Hammer, “Plecs-piece-wise linear electrical circuit simulation for simulink.” *Proc. of the IEEE 1999 International Conference on Power Electronics and Drive Systems (PEDS 1999)*, Hong Kong, July 1999.

[11] A. W. Kelly, W. R. Owens, “Connectorless Power Supply for an Aircraft Passenger Entertainment System,” *IEEE Trans. on Power Electronics*, vol. 4, no. 3, pp. 348-354, July 1989.

[12] R. Laouamer, M. Brunello, J. P. Ferrieux, O. Normand, N. Buchheit, “A Multiresonant Converter for Non-Contact Charging with Electromagnetic Coupling.” *Proc. of 23rd Int. Conf. on Industrial Electronics, Control and Instrumentation (IECON 97)*, Nov. 1997.

[13] H. Abe, H. Sakamoto, K. Harada, “A Non-Contact Charger Using a Resonant Converter with Parallel Capacitor of the Secondary Coil,” *IEEE Trans. on Industry Applications*, vol. 36, no. 2, pp. 444-451, March/April 2000.

[14] C. Auvigne, P. Germano, D. Ladas, Y. Perriard, “A dual-topology ICPT applied to an electric vehicle battery charger,” *Proc. of 20th Int. Conf. on Electrical Machines (ICEM 2012)*, Marseille (France), Sept. 2012, vol., no., pp.2287,2292.

[15] C.-S. Wang, G. A. Covic, and O. H. Stielau, “General stability criterions for zero phase angle controlled loosely coupled inductive power transfer systems.” *Proc. of the 27th Annual Conf. of the IEEE in Industrial Electronics Society (IECON 2001)*, Denver (USA), Nov./Dec. 2001 vol. 2, pp. 1049 –1054.

[16] O. Stielau and G. Covic, “Design of loosely coupled inductive power transfer systems,” *Proc. of Int. Conf. on Power System Technology (PowerCon 2000)*, Perth (Australia), Dec. 2000, vol. 1, pp. 85–90.